

# Blind Quality Assessment of Fused WorldView-3 Images by Using the Combinations of Pansharpening and Hypersharpener Paradigms

Chiman Kwan, Bence Budavari, Alan C. Bovik, *Fellow, IEEE*, and Giovanni Marchisio

**Abstract**—WorldView 3 (WV-3) is the first commercially deployed super-spectral, very high-resolution (HR) satellite. However, the resolution of the short-wave infrared (SWIR) bands is much lower than that of the other bands. In this letter, we describe four different approaches, which are combinations of pansharpening and hypersharpening methods, to generate HR SWIR images. Since there are no ground truth HR SWIR images, we also propose a new picture quality predictor to assess hypersharpening performance, without the need for reference images. We describe extensive experiments using actual WV-3 images that demonstrate that some approaches can yield better performance than others, as measured by the proposed blind image quality assessment model of hypersharpened SWIR images.

**Index Terms**—Hypersharpener, image quality, multispectral, pansharpening, short-wave infrared (SWIR), superspectral, very high resolution (VHR), visible near infrared (VNIR), WorldView 3 (WV-3).

## I. INTRODUCTION

IT IS well known that images containing more spectral bands allow for better discrimination power than images with fewer bands. For example, a red–green–blue (RGB) image enables much better discrimination capability than gray-level images.

WorldView 3 (WV-3) data include 16 bands, excluding the panchromatic band, at different resolutions (see Table I). However, when collectively analyzing or fusing this data, it would be ideal to generate 16 aligned very high-resolution (HR) images. Although many algorithms [1]–[16] have been proposed that fuse images from different bands, this field is still evolving with new algorithms introduced frequently.

In Section II, we describe four simple approaches for generating HR WV-3 short-wave infrared (SWIR) images. As part of each approach, any of a number of pansharpening algorithms

Manuscript received May 8, 2017; revised June 28, 2017 and July 22, 2017; accepted August 7, 2017. Date of publication August 24, 2017; date of current version September 25, 2017. This work was supported by the Defense Advanced Research Projects Agency under Contract D17PC00025. (Corresponding author: Chiman Kwan.)

C. Kwan and B. Budavari are with Applied Research LLC., Rockville, MD 20850 USA (e-mail: chiman.kwan@arllc.net; bencebudavari@gmail.com).

A. C. Bovik is with the University of Texas, Austin, TX 78712 USA (e-mail: bovik@ece.utexas.edu).

G. Marchisio is with the Digital Globe, Inc., Westminster, CO 80234 USA (e-mail: gmarchis@digitalglobe.com).

Color versions of one or more of the figures in this letter are available online at <http://ieeexplore.ieee.org>.

Digital Object Identifier 10.1109/LGRS.2017.2737820

TABLE I

WV-3 DATA SET INFORMATION IN THIS PAPER

Image	Number of Bands	Spectral Range (nm)	Spatial Resolution (m)	Radiometric Resolution (bit)	Dimensions (pixel)
Pan	1	400-800	0.31	11	2400 x 2400
VNIR	8	400-1040	1.2	11	600 x 600
SWIR	8	1195-2365	7.5	14	100 x 100

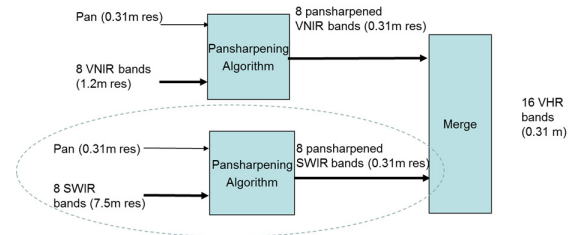


Fig. 1. Parallel one-step approach to generating HR VNIR and SWIR bands.

may be deployed. We also describe a necessary instrument to evaluate hypersharpened SWIR images, in the form of a new blind image quality assessment (IQA) algorithm, in Section III. This is an important contribution, since existing no-reference quality prediction schemes for pansharpened images [1] are only applicable to scenarios where the pan band overlaps the multispectral bands. The new quality prediction model is applicable to scenarios especially when the pan band does not overlap with the SWIR bands. Section IV describes how actual images were used to compare the performances of the various algorithms. Finally, concluding remarks and future research directions are given in Section V.

## II. FUSION APPROACHES

Some of the key WV-3 parameters are summarized in Table I. We consider four simple but effective fusion/pansharpening approaches that can be applied directly to WV-3 images. These approaches involve a combination of pansharpening and hypersharpening [17] paradigms because the HR visible near infrared (VNIR) bands are generated by pansharpening and the HR SWIR bands are generated by hypersharpening, which is the fusion of VNIR bands with lower resolution (LR) SWIR bands.

### A. Approach 1: Parallel One-Step Fusion

As shown in Fig. 1, the “parallel one-step” approach involves two parallel modules. This may be viewed as an existing, standard approach to pansharpening, wherein an HR pan band is used to enhance the other, LR bands. Module 1

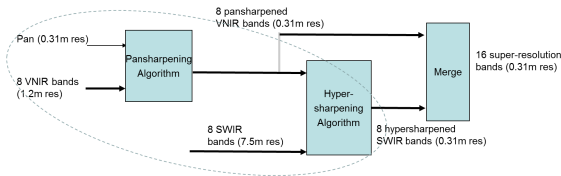


Fig. 2. Sequential fusion of pan, VNIR, and SWIR bands.

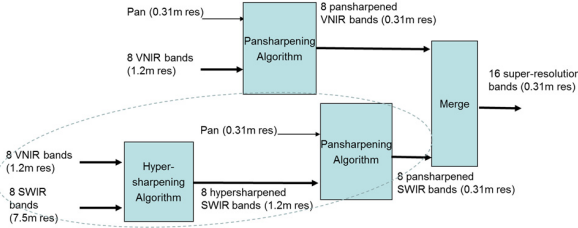


Fig. 3. Sequential-parallel fusion of pan, VNIR, and SWIR bands.

fuses the pan band with the eight VNIR bands, thereby generating eight HR VNIR bands having equal resolutions of 0.31 m. Module 2 fuses the pan band with the eight LR SWIR bands, generating eight HR SWIR bands having the same 0.31-m resolution. The outputs of Modules 1 and 2 are merged to form an HR 16-band image cube. The two modules can be executed in parallel.

### B. Approach 2: Sequential Fusion

Fig. 2 shows a sequential pansharpening method. First, the pan band and the eight LR VNIR bands are fused to generate eight HR VNIR bands, having 0.31-m resolution. Then, the eight pansharpened VNIR bands are fused with the eight LR SWIR bands to generate eight hypersharpened SWIR bands of resolutions also 0.31 m. Finally, the HR bands are merged into a single 16-band image cube.

### C. Approach 3: Sequential-Parallel Fusion

Fig. 3 depicts a sequential-parallel fusion approach. In this system, there are two parallel paths. The first path has only one step, whereby the pan band and the eight VNIR bands are fused, yielding eight pansharpened bands having 0.31-m resolution. The second path requires two steps. Step 1 involves fusing eight VNIR and eight SWIR bands to generate eight hypersharpened SWIR bands of 1.2-m resolution. Step 2 of the second path involves fusing the pan band with the outputs of step 1 to generate HR SWIR bands of 0.31-m resolution. Finally, the outputs of the two paths are merged to form a 16-band HR image cube of 0.31-m resolution.

### D. Approach 4: Parallel-Sequential Fusion

Finally, Fig. 4 illustrates a parallel-sequential fusion approach. Module 1 implements fusion of the pan band with the eight VNIR bands, while Module 2 fuses the eight VNIR with eight SWIR bands. Both modules can be executed in parallel. Module 3 then fuses the outputs of Modules 1 and 2 to generate eight HR SWIR bands. Lastly, the outputs of Module 1 and Module 3 are merged to form a 16-band HR image cube.

It should be noted that, in all the previously mentioned approaches, an optional guided filter, with the pan band serving as the reference image, could be applied to the output image of each individual module to further improve the performance.

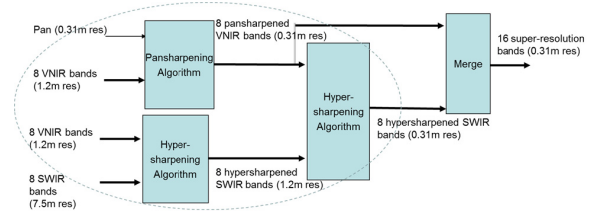


Fig. 4. Parallel-sequential fusion approach to generating HR VNIR and SWIR bands.

## III. BLIND IMAGE QUALITY ASSESSMENT

Section II described four different approaches to generating HR SWIR images. Since there are no ground truth SWIR images, it is difficult to assess which method delivers the best performance, without some objective assessment models that are widely used, e.g., in digital television and digital cameras [18]. One possible approach is to apply the Wald's protocol [7]. However, for the WV-3 images (size of SWIR is  $100 \times 100$ ), we do not have HR SWIR images at the pan resolution ( $2400 \times 2400$ ), which could be downsampled to LR images for the purpose of using the Wald's protocol. Fortunately, recent years have seen the advent of powerful no-reference IQA models and algorithms. In the remote sensed image field, some algorithms have been developed for assessing the quality of color/gray images [19], [20] and multispectral images [1], [22], where the pan band overlaps with the LR multispectral bands. For example, the model in [22] is called quality with no reference (QNR). However, to the best of our knowledge, there are no blind IQA tools suitable for analyzing SWIR images when the pan band does not overlap with the SWIR bands, which is the case for WV-3 images and many other hyperspectral sensors.

It is well known that there are both spectral and spatial distortions that arise as a consequence of the pansharpening process [1], [22]. Here, we propose a new approach that combines two complementary quality measurements, respectively, of spectral and spatial distortions. The new model is the product of a spectral distortion measurement and a spatial distortion measurement. We call this new model the generalized QNR (GQNR). We describe this model in the following sections.

### A. Spectral Distortion Metric

As described in [1], the spectral distortion measure with no reference is defined as

$$D_\lambda = \sqrt[p]{\frac{1}{N(N-1)} \sum_{i=1}^N \sum_{j=1, j \neq i}^N |d_{i,j}(MS, MS^{PS})|^p}$$

where  $d_{i,j}(MS, MS^{PS}) = Q(MS_i, MS_j) - Q(MS_i^{PS}, MS_j^{PS})$ , and  $Q(I, J) = \frac{\sigma_{IJ}}{\sigma_I \sigma_J} \frac{2\bar{I}\bar{J}}{I^2 + J^2} \frac{2\sigma_I \sigma_J}{(\sigma_I^2 + \sigma_J^2)}$ . Note that  $\sigma_{IJ}$  is a weighted local measurement of the sample covariance of  $I$  and  $J$ , and  $\bar{I}$  and  $\bar{J}$  are the means of  $I$  and  $J$ , respectively. Here,  $MS$  and  $MS^{PS}$  denote original LR images and pansharpened multispectral images, respectively, and no ground truth reference images are needed. This model is an adaptation of the well-known universal quality index [20], which in turn is a version of the Emmy-award winning structural similarity model [21].



Fig. 5. Pan image used in our experiment.

This index,  $Q(I, J)$  [20], which delivers values in the range  $[0, 1]$ , measures the degree of correlation/similarity between two images, while  $d_{i, j}$  captures the level of consistency between the original MS bands and the pansharpened bands. Hence,  $D_\lambda$  characterizes the spectral closeness between the pansharpened bands and the original MS bands. A small value of  $D_\lambda$  means that the spectral distortion is small.

### B. Spatial Distortion Metric Based on NIQE

A “completely blind” IQA model was recently developed [19] that only makes use of measurable deviations from expected statistical regularities that are observed on high-quality natural images, without the need for training on human rated distorted images, or indeed on any exposure to distorted images at all. This model, called the natural image quality evaluator (NIQE) [19], is based on the construction of a “quality aware” collection of statistical features based on a simple and successful space domain natural scene statistic model. These features are derived on a corpus of natural, undistorted images.

To assess the quality of pansharpened SWIR images, we first constructed a corpus of high-quality SWIR images, then extracted NIQE features from them to create an SWIR-specific NIQE model, as described in [19]. In application, NIQE is applied to each pansharpened band, yielding a score for that band. The average of all the scores across bands, denoted  $D_S$ , is taken as the prediction of the spatial quality of a pansharpened SWIR image cube having  $N$  bands. A small value of  $D_S$  means that the spatial quality is good.

### C. Proposed Metric for Pansharpened SWIR Images

The QNR model in [1] and [22] cannot be applied in our application, because the pan band does not overlap with the SWIR bands in WV-3 images. Hence, we created the new metric, defined as the product of  $D_\lambda$  and  $D_S$ :  $D_{\lambda S} = D_\lambda \cdot D_S$ . The use of product rule has two advantages. One is that it is fair to each metric. Another one is that it can handle high dynamic ranges. A small value of  $D_{\lambda S}$  implies that the overall quality is better. Since the new quality model is independent of the requirement of overlap between the pan band and the SWIR bands or the availability of any reference bands, we call our new model the GQNR.

TABLE II  
OBJECTIVE QUALITY SCORES ON PANSHARPENED VNIR IMAGES

Methods	QNR	Rank
HCM	0.839	4
SFIM	0.746	8
MTF_GLP	0.824	5
MTF_GLP_HPM	0.823	6
MTF_GLP_CBD	0.794	7
GS	0.895	1
GSA	0.880	3
PCA	0.891	2
GFPCA	0.723	9
Bicubic	0.690	10

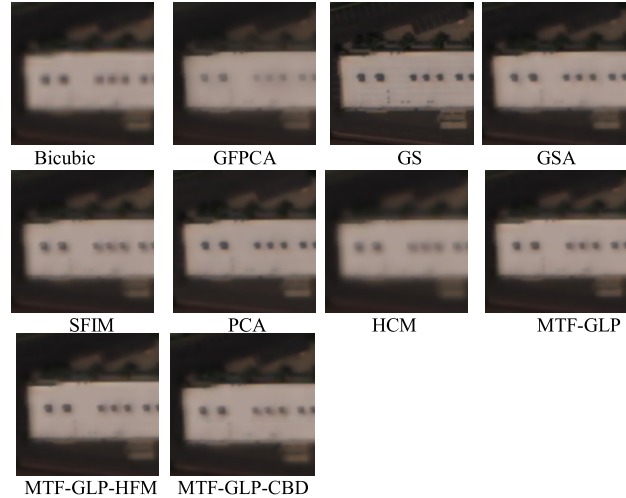


Fig. 6. Zoomed-in views of the results of different pansharpening algorithms applied on VNIR bands.

## IV. EXPERIMENTAL RESULTS

Next, we present detailed evaluation results on actual WV-3 images obtained from digital globe. One objective is to compare the performance of the four pansharpening approaches. The other objective is to see whether the proposed image quality metric described in Section III makes accurate quality predictions.

### A. Pansharpened VNIR Bands

Among the four approaches described in Section II, the generation of the VNIR bands is the same. That is, we always use the pan band to pansharpen the eight VNIR bands. Ten pansharpening algorithms were compared: principal component analysis (PCA) [2], guided filter PCA [3], Gram Schmidt (GS) [4], GS adaptive [5], modulation transfer function generalized laplacian pyramid (MTF-GLP) [6], MTF-GLP with high-pass modulation [7], MTF-GLP with contextual-based decision [1], smoothing filter-based intensity modulation [8], bicubic interpolation [9], and hybrid color mapping (HCM) [10]–[16]. The list is a representative, if not exhaustive, set of competitive pansharpening algorithms. Fig. 5 shows the pan image used in our experiment. Since the pan band overlaps with the VNIR bands, scores generated using QNR [1] can be applied, with results summarized in Table II. The ranks are determined based on the values of QNR. We also show a small section of performance of each pansharpened image to allow visual comparison of performance. In Fig. 6,

TABLE III  
PERFORMANCE RESULTS FOR APPROACH 1

Methods	$D_\lambda$	$D_S$	GQNR	Rank	Overall Rank	Computational Time (s)
HCM	0.123	39.670	4.863	10	40	7
SFIM	0.039	13.829	0.542	2	14	8
MTF_GLP	0.064	13.871	0.889	5	22	11
MTF_GLP_HPM	0.060	13.962	0.844	3	20	11
MTF_GLP_CBD	0.048	17.706	0.855	4	21	4368
GS	0.136	15.103	2.059	7	34	8
GSA	0.279	16.939	4.727	9	39	8
PCA	0.023	15.071	0.346	1	<b>11*</b>	9
GFPCA	0.080	19.795	1.576	6	33	12
Bicubic	0.090	27.711	2.503	8	35	1

TABLE IV  
PERFORMANCE RESULTS FOR APPROACH 2

Methods	$D_\lambda$	$D_S$	GQNR	Rank	Overall Rank	Computational Time (s)
HCM	0.072	13.432	0.973	5	26	45
SFIM	0.055	12.711	0.705	1	<b>17*</b>	8
MTF_GLP	0.088	14.356	1.263	8	31	10
MTF_GLP_HPM	0.090	13.355	1.206	7	30	10
MTF_GLP_CBD	0.047	17.972	0.841	3	19	3921
GS	0.090	12.560	1.134	6	29	8
GSA	0.079	12.104	0.956	4	25	9
PCA	0.061	12.561	0.764	2	18	9
GFPCA	0.077	18.100	1.398	9	32	11
Bicubic	0.090	27.711	2.503	10	35	1

the 5, 3, 2 bands were used to form an RGB image. From Table II and Fig. 6, it may be seen that the GS algorithm delivered the best performance.

### B. Fused SWIR Images

The HR SWIR images were generated using the four aforementioned approaches where all ten of the pansharpening algorithms were used. The fusion of VNIR and SWIR is done depending on the algorithms. For all the algorithms except HCM, we created a “pan” band by taking the average of all the VNIR bands. For the HCM, we directly used the eight VNIR bands to sharpen the SWIR images. To objectively investigate which approach yields the best results, we applied the GQNR model described in Section III to the hypersharpened SWIR images. Here, QNR was not applicable because the pan band does not overlap with the SWIR bands.

Although NIQE is a blind assessment algorithm, it still requires a process of training on good quality images. We therefore built a training set of nearly 200 original VNIR and pan images deemed to be of high visual quality; no pansharpened or hypersharpened images were included. During the training, the window size and sharpness threshold parameters in NIQE were chosen to be 96 with no window overlap and 0.3, respectively. After the NIQE model has been trained, the model may be applied to generate  $D_S$  scores. It should be noted that the window sizes are design parameters, which may be application dependent, and can differ in training and testing. During testing, we used a window size of 256 with an overlap of 64. For  $D_\lambda$ , there is no need for training.

Based on preliminary assessments, we observed that the GQNR scores agree well with subjective evaluations. Tables III–VI summarize the performance metrics generated using the four approaches. The first column shows the names of the various algorithms; the second to fourth columns show

TABLE V  
PERFORMANCE RESULTS FOR APPROACH 3

Methods	$D_\lambda$	$D_S$	GQNR	Rank	Overall Rank	Computational Time (s)
HCM	0.018	12.165	0.219	1	<b>1*</b>	147
SFIM	0.026	12.868	0.340	5	9	9
MTF_GLP	0.022	12.336	0.270	3	4	11
MTF_GLP_HPM	0.022	12.287	0.269	2	2	11
MTF_GLP_CBD	0.032	12.867	0.409	6	13	3863
GS	0.022	12.630	0.274	4	6	9
GSA	0.082	12.607	1.030	9	27	10
PCA	0.074	12.637	0.934	8	24	10
GFPCA	0.049	13.616	0.673	7	15	14
Bicubic	0.090	27.711	2.503	10	35	1

TABLE VI  
PERFORMANCE RESULTS FOR APPROACH 4

Methods	$D_\lambda$	$D_S$	GQNR	Rank	Overall Rank	Computational Time (s)
HCM	0.022	12.588	0.281	4	8	173
SFIM	0.026	12.868	0.340	5	10	9
MTF_GLP	0.022	12.336	0.270	2	5	12
MTF_GLP_HPM	0.022	12.287	0.269	1	<b>3*</b>	12
MTF_GLP_CBD	0.032	12.866	0.409	6	12	4084
GS	0.022	12.630	0.274	3	6	9
GSA	0.082	12.607	1.030	9	28	10
PCA	0.074	12.637	0.934	8	23	10
GFPCA	0.049	13.613	0.673	7	16	13
Bicubic	0.090	27.711	2.503	10	35	1

the  $D_\lambda$ ,  $D_S$ , and GQNR results, respectively; the fifth column shows the rank of each method based on the GQNR score; the sixth column shows the rank of each method among all the methods for each of the four approaches; and the last column shows the computational time required for each method.

From Table III, one can see that PCA yielded the lowest GQNR score and hence the best rank (highlighted in bold and with a “\*”). However, the overall rank of PCA was only 11 among all the methods among the four approaches.

One can see from Table IV that the best rank of Approach 2, 17, is lower than that of Approach 1, 11. Table V shows that the HCM method yielded the lowest GQNR score and was also the best among all approaches. By comparing the various scores and ranks in Table VI, it may be seen that Approach 4 delivered slightly inferior performance than that of Approach 3.

Since the best rank only takes into account the performance of a single method in an approach, it is also important to analyze the performance of all methods across the four approaches. Even when one compares the performance of a respective method from Approaches 1 and 2 to Approaches 3 and 4, there is a general trend of improved performance, with a few exceptions.

The computational complexity of the four approaches is quite comparable. Although one would expect Approaches 3 and 4 to have significantly longer computational times due to additional processing blocks, these additional blocks are executed very quickly. Note that these computational times do not take into account the VNIR pansharpening blocks, since all approaches employed the GS method for this step.

For subjective visualization, we used the first three bands of the fused SWIR image cube to generate a false color image. A zoomed-in view of a small section of each image is shown in Fig. 7, which only shows the GS results from each

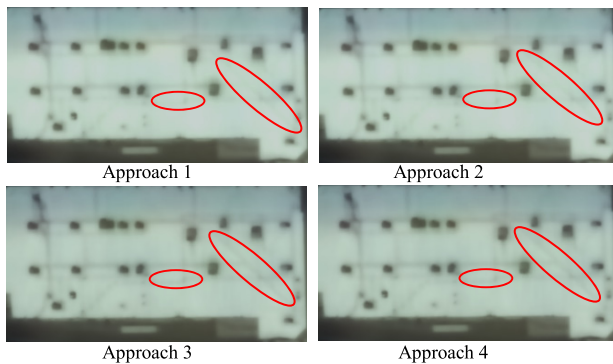


Fig. 7. Zoomed-in views of a small section of the pansharpened SWIR image cube. Only the GS results from the four approaches are shown.

approach. It can be seen that Approaches 3 and 4 gave similar visual performance while Approaches 1 and 2 were slightly inferior, as many fine details (see details inside the red circles in Fig. 7) were faint.

The above visual inspection corroborates well with the GQNR scores. Looking at the overall ranks of GS in Tables III–VI, GS of Approach 1 (rank 34) and GS of Approach 2 (rank 29) were both lower than the GS scores in Approach 3 (rank 6) and Approach 4 (rank 6). This is because the GQNR scores for GS in Approach 1 (2.059) and Approaches 2 (1.134) were worse than those of GS in Approach 3 (0.274) and Approach 4 (0.274). Although the  $D_S$  scores in Approaches 2–4 are comparable, the spectral distortion  $D_\lambda$  for Approaches 3 and 4 was much smaller. This example also highlights the value of using GQNR, which combines the distortion measures in both the spectral and spatial domains.

## V. CONCLUSION

Four ways of generating HR SWIR images in WV-3 images were studied. Using a powerful quality assessment model, it was found that the standard approach to pansharpening Approach 1 did not perform well. Two approaches (Approaches 3 and 4) performed much better than Approaches 1 and 2. The new objective IQA tool without reference for fused SWIR images was used as the basis of comparison. We believe that this new performance metric (GQNR) is the first that can blindly assess pansharpened image quality where the pan band does not overlap with the SWIR bands. Our preliminary experiments show that the fusion approaches and algorithms are promising. Our future research plans include more experiments to validate the proposed pansharpening ideas on the same class as well as other classes of satellite data, including Landsat and Hyperion, and additional systematic testing and development of IQA models for fused SWIR images where pan bands do not overlap with SWIR bands. We also plan to apply the best fused HR SWIR image generation methods to applications such as vegetation mapping, border monitoring, and surveillance.

## ACKNOWLEDGMENT

The views, opinions, and/or findings expressed are those of the author(s) and should not be interpreted as representing the official views or policies of the Department of Defense or the U.S. Government.

## REFERENCES

- [1] G. Vivone *et al.*, “A critical comparison among pansharpening algorithms,” *IEEE Trans. Geosci. Remote Sens.*, vol. 53, no. 5, pp. 2565–2586, May 2015.
- [2] P. S. Chavez, S. C. Sides, and J. A. Anderson, “Comparison of three different methods to merge multiresolution and multispectral data—Landsat TM and SPOT panchromatic,” *Photogramm. Eng. Remote Sens.*, vol. 57, no. 3, pp. 295–303, Mar. 1991.
- [3] W. Liao *et al.*, “Processing of multiresolution thermal hyperspectral and digital color data: Outcome of the 2014 IEEE GRSS data fusion contest,” *IEEE J. Sel. Topics Appl. Earth Observ. Remote Sens.*, vol. 8, no. 6, pp. 2984–2996, Jun. 2015.
- [4] C. A. Laben and B. Brower, “Process for enhancing the spatial resolution of multispectral imagery using pan-sharpening,” U.S. Patent 6011 875, Jan. 4, 2000.
- [5] B. Aiazzi, S. Baronti, and M. Selva, “Improving component substitution pansharpening through multivariate regression of MS + pan data,” *IEEE Trans. Geosci. Remote Sens.*, vol. 45, no. 10, pp. 3230–3239, Oct. 2007.
- [6] B. Aiazzi, L. Alparone, S. Baronti, A. Garzelli, and M. Selva, “MTF-tailored multiscale fusion of high-resolution MS and pan imagery,” *Photogramm. Eng. Remote Sens.*, vol. 72, no. 5, pp. 591–596, May 2006.
- [7] G. Vivone, R. Restaino, M. D. Mura, G. Licciardi, and J. Chanussot, “Contrast and error-based fusion schemes for multispectral image pansharpening,” *IEEE Trans. Geosci. Remote Sens. Lett.*, vol. 11, no. 5, pp. 930–934, May 2014.
- [8] J. G. Liu, “Smoothing filter-based intensity modulation: A spectral preserve image fusion technique for improving spatial details,” *Int. J. Remote Sens.*, vol. 21, no. 18, pp. 3461–3472, Dec. 2000.
- [9] R. G. Keys, “Cubic convolution interpolation for digital image processing,” *IEEE Trans. Acoust., Speech, Signal Process.*, vol. 29, no. 6, pp. 1153–1160, Dec. 1981.
- [10] J. Zhou, C. Kwan, and B. Budavari, “Hyperspectral image super-resolution: A hybrid color mapping approach,” *J. Appl. Remote Sens.*, vol. 10, no. 3, Sep. 2016, Art. no. 035024.
- [11] C. Kwan, J. H. Choi, S. Chan, J. Zhou, and B. Budavari, “Resolution enhancement for hyperspectral images: A super-resolution and fusion approach,” in *Proc. IEEE Int. Conf. Acoust., Speech Signal Process. (ICASSP)*, New Orleans, LA, USA, 2017, pp. 6180–6184.
- [12] M. Dao, C. Kwan, B. Ayhan, and J. F. Bell, “Enhancing mastcam images for mars rover mission,” in *Proc. 14th Int. Symp. Neural Netw.*, Hokkaido, Japan, 2017, pp. 197–206.
- [13] C. Kwan, B. Budavari, M. Dao, B. Ayhan, and J. Bell, “Pansharpening of mastcam images,” in *Proc. IEEE Int. Geosci. Remote Sens. Symp.*, Fort Worth, TX, USA, 2017, pp. 5117–5120.
- [14] C. Kwan, B. Budavari, and F. Gao, “A hybrid color mapping approach to fusing MODIS and landsat images for forward prediction,” *MDPI J. Remote Sens.*, submitted for publication.
- [15] C. Kwan *et al.*, “A super-resolution and fusion approach to enhancing hyperspectral images,” *IEEE J. Sel. Topics Appl. Earth Observ. Remote Sens.*, submitted for publication.
- [16] C. Kwan, B. Ayhan, and B. Budavari, “Fusion of THEMIS and TES for accurate mars surface characterization,” in *Proc. IEEE Int. Geosci. Remote Sens. Symp.*, Fort Worth, TX, USA, 2017, pp. 3381–3384.
- [17] M. Selva, B. Aiazzi, F. Butera, L. Chiarantini, and S. Baronti, “Hypersharpening: A first approach on SIM-GA data,” *IEEE J. Sel. Topics Appl. Earth Observ. Remote Sens.*, vol. 8, no. 6, pp. 3008–3024, Jun. 2015.
- [18] A. C. Bovik, “Automatic prediction of perceptual image and video quality,” *Proc. IEEE*, vol. 101, no. 9, pp. 2008–2024, Sep. 2013.
- [19] A. Mittal, R. Soundararajan, and A. C. Bovik, “Making a ‘completely blind’ image quality analyzer,” *IEEE Signal Process. Lett.*, vol. 22, no. 3, pp. 209–212, Mar. 2013.
- [20] Z. Wang and A. C. Bovik, “A universal image quality index,” *IEEE Signal Process. Lett.*, vol. 9, no. 3, pp. 81–84, Mar. 2002.
- [21] Z. Wang, A. C. Bovik, H. R. Sheikh, and E. P. Simoncelli, “Image quality assessment: From error visibility to structural similarity,” *IEEE Trans. Image Process.*, vol. 13, no. 4, pp. 600–612, Apr. 2004.
- [22] L. Alparone *et al.*, “Multispectral and panchromatic data fusion assessment without reference,” *Photogramm. Eng. Remote Sens.*, vol. 74, no. 2, pp. 193–200, Feb. 2008.